X-ray emission and transport in gold plasmas generated by 351-nm laser irradiation

H. Nishimura, H. Takabe, K. Kondo, T. Endo, H. Shiraga, K. Sugimoto,
T. Nishikawa, Y. Kato, and S. Nakai
Institute of Laser Engineering, Osaka University, 2-6, Yamadaoka, Suita, Osaka 565, Japan
(Received 1 June 1990; revised manuscript received 13 November 1990)

Emission and transport characteristics of sub-keV x rays in laser-produced gold plasmas are investigated. Absolute x-ray spectra under three different experimental conditions have been measured with high spectral resolution to study dependences of x-ray emission on laser incidence angles, irradiation intensity, and thickness of a foil target. Simulations by a one-dimensional hydrodynamic code, which incorporates a detailed atomic physics, replicate quite well the general x-ray emission features obtained in the experiments. There remain, however, discrepancies in some details of spectral shapes, notably in the range between 0.5 and 0.9 keV. It is also shown that the transport of radiation heat wave deduced from x-ray emissions at the front and the rear sides of a thin gold foil may be interpreted by the self-similar solutions presented by Pakula and Sigel [Phys. Fluids. **28**, 232 (1985); **29**, 1340 (E) (1986)] with an approximated gold opacity under local thermodynamic equilibrium.

I. INTRODUCTION

Interaction of laser light with high-Z materials provides an attractive subject for investigation into radiation hydrodynamics and the atomic physics of hot dense matters. Considerable work has been made in order to understand various aspects of x-ray conversion and transport. It has become generally understood that short-wavelength laser irradiation on high-Z materials at moderate intensities leads to high x-ray conversion.[1,2] The detailed aspects of radiation transport in dense high-Z plasmas, however, have not been completely clarified.

The approach to investigating this subject generally involves the comparison of experimental results with numerical simulations. Through these comparisons the physical models are systematically refined in order to make the code reliable enough to estimate the phenomena which will occur in an extended region. One difficulty of this approach is that the planar target experiments are affected by lateral energy transport and plasma expansion, particularly when the laser spot size is small. It has been observed that the instantaneous ratio of the emitted x-ray flux to the laser flux deposited in the target increases throughout a laser pulse of long duration. This increase has been ascribed to soft x rays emitted from the plasma outside of the laser spot.[3] Mead *et al.*[1] carefully treated this two-dimensional (2D) effect with a 1D code for a divergent geometry in the calculation code. This lateral effect has been eliminated in uniform irradiation of a spherical target with multiple laser beams.[4] General features of the x-ray spectra and the dependence of the x-ray conversion rate on the laser intensity have been well replicated by detailed computer simulations. However, detailed spectral structures and time variation of the x-ray emission still have not been well reproduced.[1,4]

In previous works, spectrometers of relatively broad bandwidth (typically $\varepsilon/\Delta\varepsilon=3$ at the photon energy of $\varepsilon=0.8$ keV for the case of filtered x-ray diodes) were used for measurement of absolute x-ray emission from laser plasmas. Uncertainty in the absolute value of the spectra was introduced in the data analysis due to the broad response function of the x-ray detectors. That is, a deconvolution procedure had to be performed by using spectra predicted by a computer code[1] or measured with relatively calibrated spectrometers.[5] Recently a transmission grating spectrometer was developed for absolute measurement of complicated x-ray-emission spectra with a higher spectral resolution of $\varepsilon/\Delta\varepsilon=8$ at $\varepsilon=0.8$ keV.[6]

In this paper we present detailed studies on modeling and measurements of x-ray emission and transport in high-Z laser-produced plasmas. Absolute measurements of temporally, spectrally, and spatially resolved x-ray emission from gold plasmas were made upon irradiation with intense blue laser light.

Results of three experiments, which we have conducted in clarifying several important aspects of the problems, are presented. First, dependence of laser absorption and x-ray emission on the incidence angle of a laser beam on a planar gold target is given. This measurement was made in order to find the range of the incidence angle at which the efficient x-ray conversion is obtained.

Second, we show the absolute spectra of the x-ray emitted from a gold-coated spherical target which was irradiated uniformly with 12 laser beams. Dependence of the spectrum on the laser intensity is shown. Our results agree well with the previous results obtained under the similar configuration.[4]

Third, a study on x-ray emission from a thin solid gold foil heated from one side of the foil is presented. X-ray emission at the front and the rear sides of the foil of varying thickness was measured. X-ray radiation emitted at the rear side of the thin foil heated by intense light[7,8] or by x-ray radiation[9] provides important information on radiation heat waves. In addition, there is a possibility that

the x-ray radiation emitted at the rear side of a laser-irradiation high-Z foil may be useful as an x-ray source if high x-ray conversion at the rear side is achieved.

The experimental results were compared with hydrodynamic code ILESTA calculations. The code includes multiple-group radiation transport and non-local thermodynamic equilibrium (LTE) average-ion-model atomic physics. It will be shown that the major features of the observed spectra can be attributed to radiative transitions to the energy levels with the principal quantum numbers $n=6$ (P lines), $n=5$ (O lines), and $n=4$ (N lines) from respective upper levels, e.g., for the P lines, the upper levels are at $n=7,8,\ldots,10$. We consider $n=10$ as the highest level. The energy of the x-ray emission integrated over the spectral range covering these components is well reproduced by the simulation. However, there remain some discrepancies in detailed spectral shapes, particularly in the N-band emission around 0.8 keV. Validity of the model used for opacity evaluation in this spectral region will be discussed.

In addition to the numerical simulation, x-ray emission at the front and the rear sides of the thin gold foil is analyzed by using the self-similar solutions[10] for radiative heat transport incorporating a scaling law for the gold opacity.[11]

This paper is organized as follows. Section II describes the modeling adopted in the present computer code and presents a few remarks important for the treatment of radiation transport and the interpretation of the experiments. In Sec. III we describe the experimental method and the results. Analysis of radiation transport observed in a thin gold foil will be presented in Sec. IV, followed by concluding remarks in Sec. V.

II. SIMULATION MODEL

Hydrodynamics which is strongly coupled with thermal x-ray radiation has been studied intensively in astrophysics and is called "radiation hydrodynamics.[12] However, the particular aspect of the radiation hydrodynamics in laser-produced plasmas is that the mean free path of the radiation may be comparable to the characteristic scale length of the plasma and that non-LTE physics of high-Z plasmas have to be treated in this situation. Therefore, a kinetic treatment of radiation transport with non-LTE opacities and emissivities is essential in order to model the phenomena considered in the present work.

Plasmas produced by laser irradiation are assumed to be adequately described by a one-fluid and two-temperature (electron temperature T_e and ion temperature T_i) model. The one-dimensional fluid ILESTA-1D, which was used for simulating direct implosion dynamics,[13] was used. Laser absorption is calculated from mesh to mesh by the method of ray tracing. Inverse-Bremsstrahlung absorption with the Coulomb logarithm of Ref. 14 is assumed. Electron heat transport controls substantially the electron temperature in the region heated by laser absorption, and consequently the x-ray-conversion rate.[1] In the present code, the flux-limited diffusion model with the limited flux $q_L=fn_e v_t T_e$ is used by assuming the net flux q_e of the form $q_e^{-1}=q_{\mathrm{SH}}^{-1}+q_L^{-1}$, where f is the flux limiting factor, n_e is the electron density, v_e is the electron thermal velocity, and q_{SH} is the Spitzer-Härm heat flux.[15] In the present paper, we employed a value of $f=0.08$ with which the x-ray-conversion rate is well reproduced by the present code. This is consistent with the work reported by Goldstone *et al.* which was analyzed with the LASNEX code.[4]

Radiation transport is solved with the multiple-grouped flux limited diffusion model.[16] The photon energies up to 3 keV are calculated with 100 equally divided groups. The maximum value of 3 keV is chosen so that the M-band x ray of gold plasma around 2.5 keV can be included in the simulation.

The modeling of the emissivity η^ν and the opacity χ^ν is a key element in the simulation of radiation transport in high-Z plasmas. We have used the screened hydrogenic model[17] for describing electronic states of the partially ionized gold atom. We have, used a modified version of the model published by More.[18] With this model, we have to determine the population of electrons at each bound state and the number of free electrons. For example, when a gold foil is heated by laser light at an intensity exceeding 10^{14} W/cm^2, the plasma near the critical density is heated to a temperature above a few keV. In the LTE model, the M shell starts stripping around 500 eV and this unphysically enhances M-band emission. In practice, the radiative deexcitation plays a dominant role to avoid the stripping of the M-shell electrons. For the determination of the electron state, the collisional-radiation model is thus more appropriate in the present situation, and we have used this model.

Coefficients summarized in Ref. 19 are used for collisional and radiative processes. In addition, dielectronic recombination, which is important at low density and high temperature, is also included.

The spectral emissivity and opacity consist of the contribution from the three processes; i.e., free-free, bound-free, and bound-bound processes. The free electrons are assumed to be in local thermodynamic equilibrium. The forms of the emissivity and the opacity given in Ref. 11 are used. In estimating the emissivity and opacity for the bound-bound process, there are a lot of outstanding issues on how to model a line shape. In the present code, we followed the method associated with the LTE opacities as described in Ref. 11. In the simulation, we have used the effective linewidth $\Delta\nu$ as an adjustable parameter, with which we can reproduce the laser-intensity dependence of the x-ray-conversion rate for the experiment reported in Ref. 4. For the case of gold, we used an effective width of $\Delta\nu=150$ eV. More details of the simulation modeling will appear elsewhere.

III. EXPERIMENT

Absolute x-ray-emission spectra were measured under three different conditions. First we describe experimental apparatuses common to all the measurements, and describe later the experimental conditions and methods particular to the three respective cases.

A. Laser

The laser was the frequency-tripled (351 nm in wavelength) light from the Gekko XII neodymium-doped glass laser facility.[20] Twelve laser beams are arranged in a two-bundled illumination configuration. Two beams are on the axis of symmetry as shown in Fig. 1, which we will call axial beams hereafter. Five additional beams on either side are aligned conically with equiangular distribution. The cone half-angle is 50°. The focal length of the final focusing lens is 93.7 cm at 351 nm with the f number of 3.0. The laser-pulse wave form at 351 nm, which was monitored for each shot with a streak camera, can be closely approximated by a Gaussian shape except for the rising and falling tails. The full width at half maximum of the pulse was typically 750±50 ps at 351 nm. The laser energy per beam was varied from 30 to 500 J.

B. Diagnostic instruments

The main diagnostic instruments were transmission grating spectrometers (TGSM's), each of which was coupled with either absolutely calibrated x-ray film for time-integrated measurements or an x-ray streak camera for time-resolved measurements. The gratings were made of gold of 0.4-μm thickness with 1000 lines/mm pitch mounted on a pinhole disk or on a slit plate. The diameters of the pinhole were 25 and 50 μm. These pinhole gratings were used for film recording in order to provide absolute x-ray spectra with 1D spatial resolution. Since the gratings were positioned at the half distance between the target and the recording film, the spatial resolution was typically 50 μm for the 25-μm-diam pinhole. Spectral resolution was typically 2 Å except for the cases noted. The observable spectral range was from 10 to 248 Å, corresponding to the photon energy range from 50 to 1240 eV. The total x-ray-emission energy was determined by integrating over this spectral range.

The time-integrated x-ray fluence E_x at the photon energy ε (keV) per unit surface area on the source, per unit solid angle ($d\Omega$), and per unit energy ($d\varepsilon$) is given by the following relation:

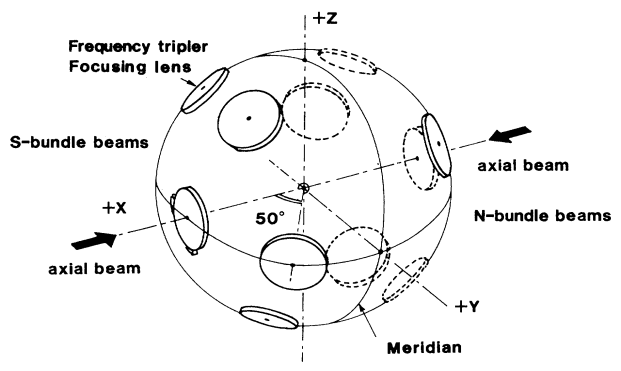

FIG. 1. Layout of two-bundled illumination system used in the experiment. Five laser beams on each side are aligned conically at the cone half-angle of 50°. Two beams lie on the axis of symmetry.

$$\frac{\partial^2 E_x}{\partial\varepsilon\partial\Omega}=1.59\times10^2\frac{l_1^2 l_2\int N\,dy}{\pi a^2 dS\eta_d\varepsilon}\ \ (\mathrm{J/keV\,cm^2\,sr})\,, \qquad (1)$$

where l_1 (cm) and l_2 (cm) are the distances from the target to the grating and from the grating to the film, respectively, N (photons/μm^2) is the photon number density on the film, y (μm) is the spatial coordinate on the film perpendicular to the dispersion direction, a (μm) is the grating aperture diameter, d (μm) is the grating pitch, S (cm^2) is the area of the source, and η_d is the diffraction efficiency of the grating.

The slit grating (50 μm in width and 800 μm in height) was used with a streak camera to obtain time-resolved measurement. The photocathode of the camera was 300-Å-thick gold evaporated on a 1000-Å parylene foil. Time resolution of the system was 20 ps and the spectral resolution was 3 Å. The absolute spectral response of this detection system was calibrated against he pinhole TGSM by using the x-ray emission from the same targets.

The recording film was Kodak Type 101-07 soft x-ray film. Absolute calibration of the film was performed by using both a pulsed-x-ray source from a laser-created plasma[6,21] and a continuous wave (cw) x-ray source from an x-ray tube. The calibrated curve, however, does not agree with the results obtained by Henke *et al.*,[22] although the same type of film and the same numerical aperture (a value of 0.1) of the densitometer were used. This might be mainly due to differences in the film production batch. We used a fitting formula to the calibrated data points assuming the thin emulsion model.[23]

The diffraction efficiency of each grating was measured by using the x-ray tube and a gas flow counter. Gratings which have a fractional energy in the higher harmonic component of less than 8% of the first-order component were used for the measurements.

The energy absorbed in the target was measured with 40 channel plasma calorimeters[24] distributed over the inside surface of the target chamber. For a planar target, the absorbed energy was derived from the calorimeter measurement assuming the axial symmetry around the target normal.

X-ray images were taken with four pinhole cameras (XPHC's) which were attached with the same Be (50-μm-thick), Al (7.5-μm-thick), and Ti (5-μm-thick) combination filters to cover the spectral range from 1 to 4 keV. The spatial resolution was better than 12 μm.

C. Incidence-angle dependence of laser light absorption and x-ray conversion

We have measured dependences of the laser absorption rate and the x-ray-conversion rate on the laser incidence angle for gold planar targets at the fixed laser intensity of 1.2×10^{15} W/cm^2. Each of the clustered beams at one side was used to irradiate the target to provide the incidence angle of 20°, 35.5°, 50°, 58.5°, and 70°. The range of the incidence angle for each case was 9.5° of a cone half-angle. The target and the spectrometers were geometrically fixed and only the laser beam fired was changed to vary the incidence angle, except for the case

of 50° incidence. The observation angle of the spectrometer from the target normal was 10° for the 20°, 35.5°, 58.5°, and 70° incidence and was 30° for the 50° incidence.

The laser energy was fixed at 312±6 J. Due to oblique incidence to the target, the laser spot was of an elliptic shape whose ellipticity varied for different incidence angles. In order to keep the irradiance constant, the focal position of the laser beam was displaced in accordance with the change in the incidence angle. The spot size, defined as the average of the major and the minor axes of the ellipse, was 206 μm. The polarization of the laser beam was different depending on the incidence angle. However, we can exclude the effect of the resonance absorption, considering the $I\lambda^2$ scaling[25] for the present value of 1.5×10^{14} W μm^2/cm^2 and the pulse duration of approximately 1 ns, where I is the laser intensity and λ is the laser wavelength.

Figure 2 shows the observed spectra for each incidence angle. Note that the spectral fluence is the value obtained at the observation angle and not the value converted to the target normal. The spectral fluence is normalized by the absorbed laser energy E_{abs}. The relative shape of the spectra did not vary greatly but the total amount of the x-ray emission decreased with the incidence angle, particularly at the angle larger than 50°. This reduction can be also seen in Fig. 3, which shows the absorption and x-ray-conversion rates as a function of the incidence angle. In this case, the total x-ray energy was determined by assuming the Lambertian distribution (i.e., cosθ angular distribution, where θ is the angle measured from the target normal). The absorption and the conversion rates are nearly constant up to 50°, above which they decrease with an increase in the incidence angle.

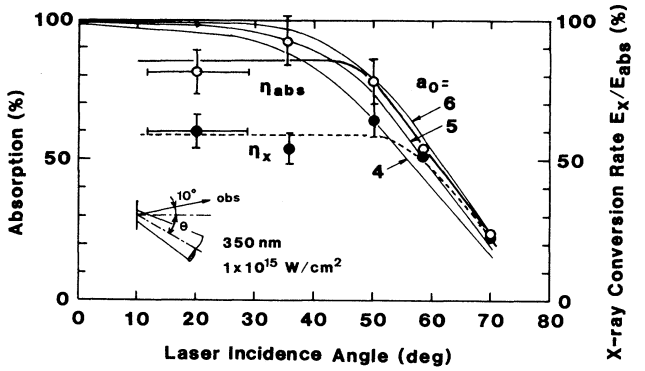

FIG. 3. Laser light absorption and x-ray-conversion rates vs laser incidence angle. The thin solid lines represent the calculated absorption rate for three different absorption parameters a_0 (see the text).

D. X-ray emission from spherical targets

Gold-coated solid sapphire (Al_2O_3) spheres were irradiated with 12 laser beams. Thickness of the Au overcoating was 1±0.1 μm and the diameter of the target was 250 μm. The focal point of the laser was displaced four radii beyond the target center. Since the beam layout of the illumination system is not spatially symmetric, the irradiation intensity close to the "meridian" (see Fig. 1) was weaker than that in the axial region by about 30% of the average value. Therefore, the effective laser intensity was estimated from an x-ray pinhole image of the spectral range from 1 to 4 keV on the assumption that the x-ray-emission intensity is proportional to the laser irradiance.

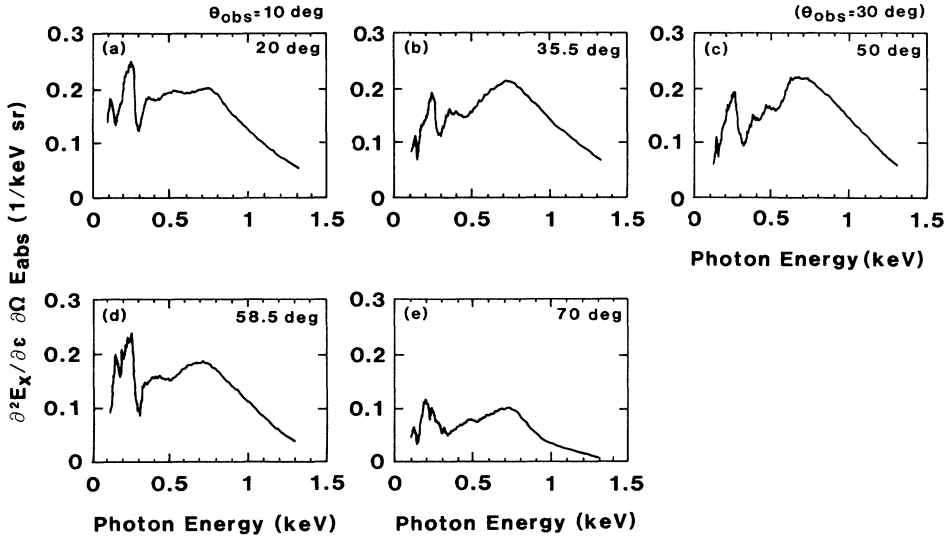

FIG. 2. X-ray-emission spectra from gold planar targets irradiated at different laser incidence angles. The observation angle with respect to the target normal was fixed at 10° except for the 50° incidence. The laser intensity was 1.2×10^{15} W/cm^2.

Total laser energy was varied from 370 to 2300 J to yield irradiances of 3.5×10^{14}, 9.9×10^{14}, and 1.6×10^{15} W/cm^2. X-ray spectra were measured at the angle of 30° from the axial beam.

Time-integrated spectra for three different cases are shown in Fig. 4. It is seen that each spectrum consists of three humps, located at around 0.15, 0.25, and 0.8 keV, and two dips between them located at around 0.2 and 0.3–0.4 keV. The ratio of the radiant energy in the higher-energy hump to that in the lower-energy hump increased markedly with the increase of the laser intensity.

The spectrum calculated with the ILESTA code for each intensity is also plotted in Fig. 4. It is seen that the spectrum is mainly composed of two emission bands corresponding to the *O*-shell transition lines located at around 0.25 keV, and to the *N*-shell lines, located at around 0.8 keV. Since the energy width of the smoothing process performed in the calculation was 0.15 keV, the fine structure of the emission arising from the *P*-shell transitions is not clearly seen. With increase in laser intensity, ionization proceeds and the population density of ions in the $n=4$ level becomes less. Hence the transition from the upper levels to the $n=4$ level becomes dominant, and the *N*-band emission becomes more intense at higher irradiances.

The spectral shape of the *N*-band emission in the ILESTA calculation is higher and narrower in comparison with the experimental observation. However, good agreement with the measurement is obtained for the total emission energy. The open circles in Fig. 5 show the x-ray-conversion rates obtained with the spherical target in the present measurement. Spectral integration was made from 0.1–1.2 keV in this case. For comparison, results from the identical experiment with 351-nm-wavelength 24-beam irradiation[4] are also plotted by the solid circles. Note that the integration range for this experiment was 0–2 keV. Considering from the spherical shape obtained by us, however, the fractional x-ray energy involved in the 0–0.1 and 1.2–2.0-keV regions might be less than 10% of the total value. Close agreement between our results and that from the 24-beam irradiation is evident. Although our laser irradiation was not completely uniform, x-ray emission toward the spectrometer was not seriously affected by the low-irradiance region, since the spectrometer axis was oriented at 30° with respect to the axis of the axial beams.

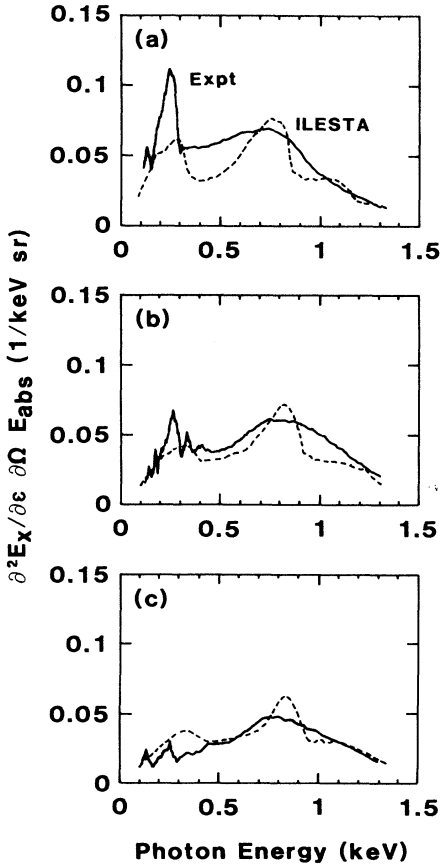

FIG. 4. X-ray-emission spectra from gold-coated spherical targets at laser intensities of (a) 3.5×10^{14}, (b) 9.9×10^{14}, and (c) 1.6×10^{15} W/cm^2. Dashed lines are the spectra calculated by the ILESTA code.

E. Radiation transport in a thin gold-foil target

We present measurements on absolute x-ray spectra emitted at the front and rear sides of a thin gold-foil target. First, dependence of the x-ray spectra on the foil thickness irradiated with a relatively small laser spot is described. Second, the x-ray spectra at both sides irradiated with a larger laser spot in order to diminish lateral effects arising from the finite spot size is reported.

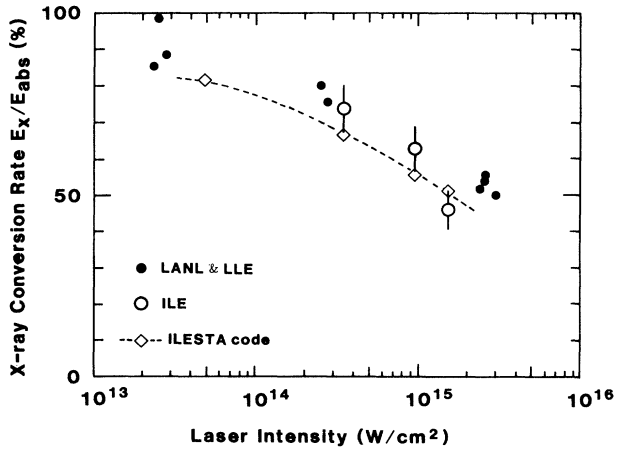

FIG. 5. X-ray-conversion rate derived from the spherical target irradiation. Good correspondence is seen between the present experiment and the ILESTA simulation as well as the result obtained from the similar experiment performed by a joint team (Ref. 4) of Los Alamos National laboratory (LANL) and Laboratory for Laser Energetics (LLE) of University of Rochester.

1. Small-spot case

The experiment was performed with either one of the two opposing axial laser beams. The experimental layout is shown in Fig. 6(a). The target normal was aligned along the laser axis and the two laser beams were used alternatively for successive shots. Two sets of equivalent diagnostic instruments were used to acquire the x-ray-emission data from the front and rear sides of the target at different but almost identical irradiation conditions. The laser energy was 160±25 J and the focal spot diameter was 430 μm, yielding an irradiance of $1.5\pm0.2\times10^{14}$ W/cm^2 onto the target. Targets were 0.1–1.2-μm-thick gold foils whose thicknesses were measured to an accuracy of less than 0.05 μm by means of the x-ray fluorescence attenuation method.

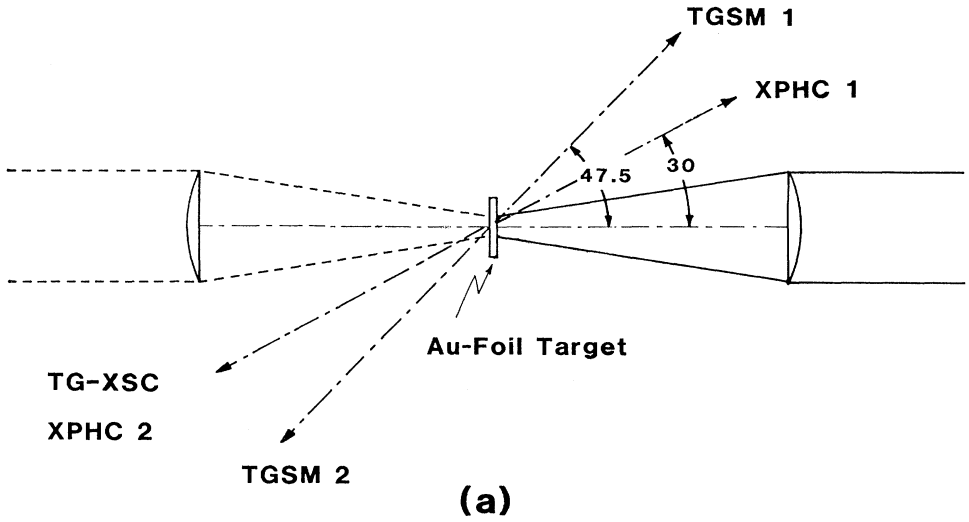

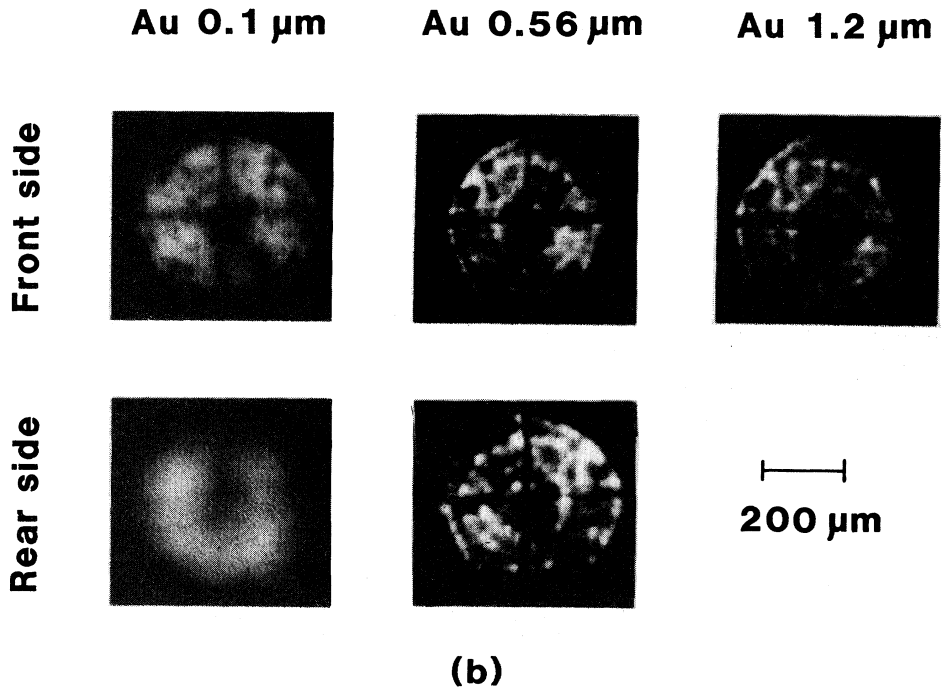

FIG. 6. (a) Experimental setup for thin gold-foil irradiation with a relatively small size of laser spot (430-μm diam). Laser intensity was 1.5×10^{14} W/cm^2. Diagnostic instruments were transmission grating spectrometers with film (TGSM's), a transmission grating with an x-ray streak camera (TG-XSC), and the x-ray pinhole camera (XPHC). The two laser beams were used alternatively throughout the shot sequence. (b) X-ray pinhole pictures at the same irradiation for three different foil thicknesses. X-ray spectral range was 2–4 keV.

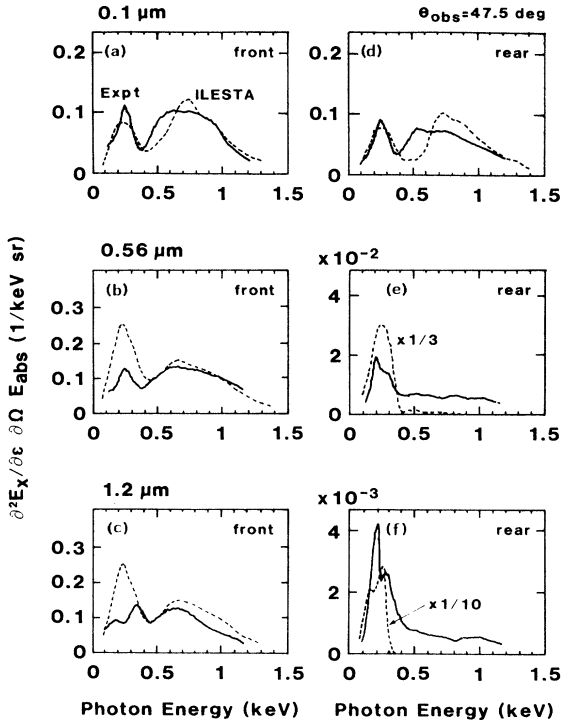

FIG. 7. Time integrated x-ray spectra observed at the front and rear sides of thin gold foils for the small-laser-spot case. Dashed lines show the simulation results. For comparison, simulated spectral intensities at the rear side for 0.56- and 1.2-μm foils are multiplied by $\frac{1}{3}$ and $\frac{1}{10}$, respectively.

Time histories of the x-ray spectra were obtained with a transmission grating coupled with an x-ray streak camera (TG-XSC) having 6.7-Å spectral resolution. The resolution is determined mainly by the spatial extent of the emission region. Fine structures of the spectral shape were lost due to this limitation. Triggering jitter of the streak camera relative to the laser peak was carefully checked with separate laser shots, and found to be within ± 50 ps. Two identical time-integrated spectrometers [TGSM-1 and TGSM-2 in Fig. 6(a)] were placed in opposite directions with respect to the target, as shown in the figure. Two XPHC's were used to monitor the intensity distribution of the laser spots.

Figure 6(b) shows typical x-ray pinhole images at the front and rear sides of the target for three different foil thicknesses. The observed energy range was 2–4 keV. A dark cross on the laser spot corresponds to the low-intensity region caused by the segmented mechanical structure of the frequency-tripling crystal arrays incorporated into the target illumination system. In addition, many hot spots appeared at both sides of the target. The typical separation distance between the hot spots is 30 μm. The estimated illumination nonuniformities caused by these hot spots are nearly 50% of the average intensity. We can identify one-to-one correlations between the hot spots on the front and rear sides of the target. Somewhat diffuse images were observed for the thinnest target. This may be due to motional blurrying of the radiator during laser illumination.

Figure 7 shows the time-integrated x-ray spectra for foils of 0.1-, 0.56-, and 1.2-μm thickness. The observed spectra from the front and rear sides of the target are shown by the solid curves, and the spectra predicted by the ILESTA simulations are shown by dashed curves. Spectral broadening of the measurement is taken into account in the simulation. For the 0.1-μm case, the spectral shapes observed from both sides of the target are very similar to each other, but the radiant energy at the rear side was about two thirds of the energy at the front side. With an increase in the foil thickness, the emission intensity at the front side increased slowly. In contrast,

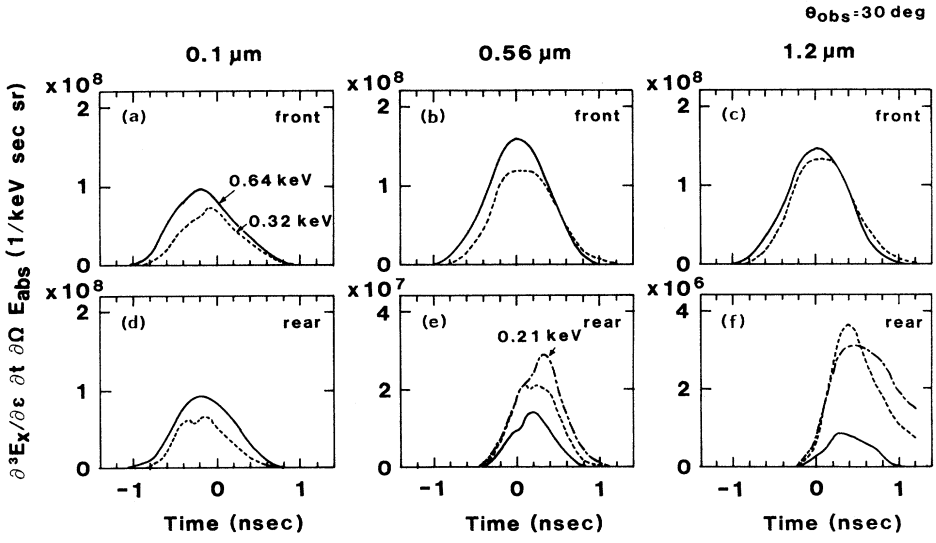

FIG. 8. Temporal variations of the x-ray emission at 0.64, 0.32, and 0.21 keV are shown for the small-spot case. With increasing foil thickness, emission from the rear side emerged at later time and duration became shorter due to the propagation time of the radiation heat wave.

the emission intensity at the rear side became weaker very rapidly with the foil thickness. Moreover, the higher-energy components decreased more rapidly than the lower-energy components. These features are also seen in Fig. 8, where time variations of the x-ray emission at $\varepsilon=0.64$, 0.32, and 0.21 keV are plotted. For the 0.1-μm-thick case, x-ray emission from both sides appeared almost simultaneously, and their intensities become maximum at about 200 ps prior to the laser peak. The observation suggests the occurrence of the laser burning through at this foil thickness. With increasing foil thickness, emission from the rear side appears later and lasts for a shorter duration.

For the front-side emission, a large discrepancy between the experiment and the simulation is seen in the *O*-band emission, as shown in Fig. 7. This may be attributed to the lateral heat conduction effect. In fact, the emission from the spherical target and that from the planar target irradiated with a larger focal spot laser (this experimental evidence is presented below) show closer agreement between the experiment and the simulation.

For the rear-side emission from the thicker foils, the *O*-band emission intensity from the calculation is much larger than that of the experiment. This relation is reversed for the *N*-band emission. In order to compare the spectral shapes relatively, the calculated emission intensity is plotted in Fig. 7 multiplied by $\frac{1}{3}$ and $\frac{1}{10}$ for the 0.56 and 1.2-μm-thick cases, respectively.

For the 0.1-μm case, burning through of the target occurs in the simulation and 37% of the incident laser energy is transmitted. Then the effective pulse duration for this target is shortened to 0.45 ns.

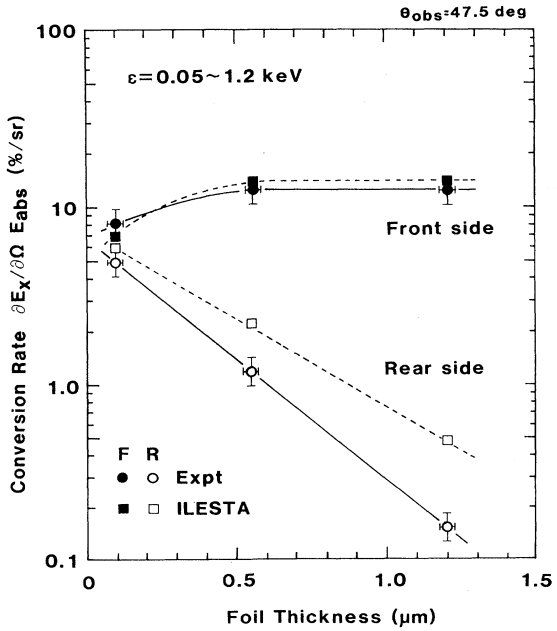

FIG. 9. X-ray conversion rate as a function of foil thickness at the front and rear sides of thin gold foils. Simulation results agree well with the experiment except for the rear-side emission from the thicker targets.

A soft x-ray conversion rate was inferred from the time-integrated spectra. Spectral integration was performed from 0.05 to 1.2 keV in this case. Results are plotted in Fig. 9 as a function of the foil thickness. A high conversion rate of ~5%/sr at the rear side is noteworthy for the 0.1-μm case; this corresponds to a conversion rate of 23% assuming the Lambertian distribution.

2. *Large-spot case*

Each bundle of the six beams alternatively irradiated a gold foil to produce a plasma of large lateral extent. The layout of this experiment is shown in Fig. 10. The target normal was aligned along the axial beam direction, and the incidence angle of the five beams surrounding the axial beam was 50°. As shown in the inset in Fig. 10, the plasma consisted of a higher-intensity region of 1.0-mm diameter, and a lower-intensity region of 1.55-mm diameter surrounding the central part. The laser energy was 440±40 J per beam. Therefore, the laser intensity at each region was $3.3\pm0.2\times10^{14}$ W/cm^2 and $1.0\pm0.1\times10^{14}$ W/cm^2, respectively. The target was a 0.436-μm-thick gold foil.

A slit plate was located on the line of sight of the spectrometer at a distance of 1.1 cm from the target to attain higher spectral resolution. The slit plate was made of a 25-μm-thick Ta and the slit width along the dispersion direction was 200 μm, allowing a 2.0-Å spectral resolution. X-ray emission from the central portion of the plasma passing through the slit was thus selected for the observation. Except for this modification, diagnostic instruments identical to those used in the small-spot experiments were oriented at 30° from the target normal.

Figures 11(a) and 11(b), respectively, show typical time-integrated emission spectra at the front and rear sides of the foil. Three humps and two dips in the spectra are evident, as seen for the spherical targets. However, the peak of the higher-energy component in the present

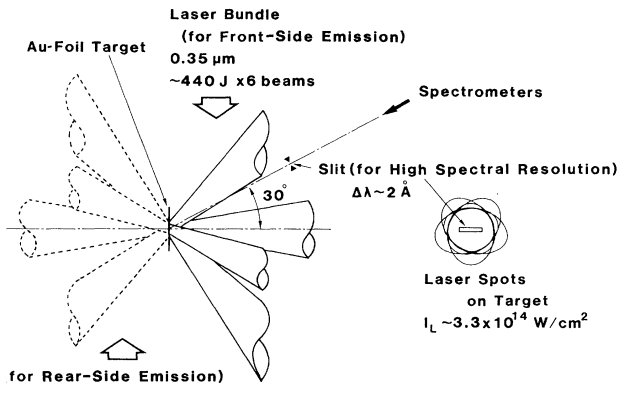

FIG. 10. Experimental setup for thin gold-foil irradiation in a large laser spot (1-mm diam). One of each beam bundle was alternatively used for each shot. A slit plate was installed on the line of sight of the spectrometers to provide high spectral resolution.

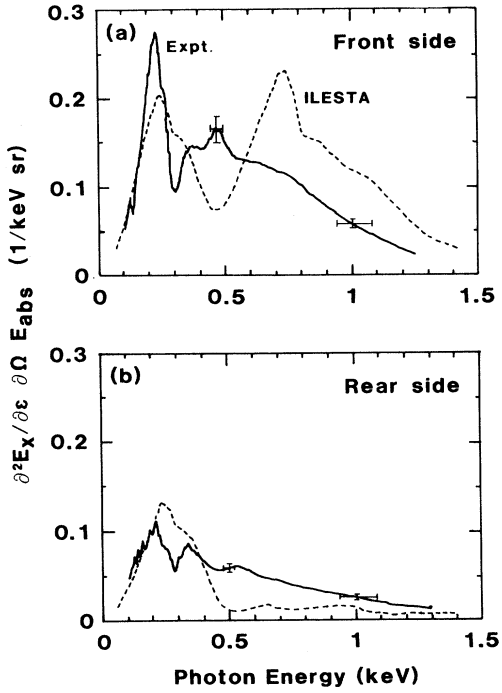

FIG. 11. Time-integrated x-ray-emission spectra at the front side (a) and the rear side (b) of the thin gold foils irradiated with a large laser spot. A discrepancy between the experiment and the simulation is seen for the N-band emission.

case is shifted toward the lower-energy side at around 0.5 keV.

The calculated emission spectra at the front side and the rear side are shown, respectively, by the dashed curves in Figs. 11(a) and 11(b). As noted for the small-spot case, better agreement is seen between the experiment and the simulation for the O-band emission. The calculated N-band emission at the front side has a sharp and narrow structure and its maximum intensity is larger than the observed x-ray intensity. By contrast, the rear-side N-band emission is much lower than the measured values.

Figure 12 shows temporal variations of the emission spectra at 0.25 and 0.83 keV which represent the O-band and N-band emissions. Emission from the rear side emerges approximately 200 ps later and rises more sharply compared with the emission from the front side. These features are well replicated in the simulation as seen in Fig. 12. X-ray intensity was derived by integrating the calculated spectrum up to 1.5 keV. A detailed discussion about the emissions derived by analytical means is presented below.

IV. DISCUSSION

A. Angular dependence of laser absorption and x-ray conversion

The absorption and x-ray conversion are sensitive to the incidence angle of the laser beam, as seen in Fig. 3. The obliquely incident electromagnetic wave is reflected at a lower-density region. The major part of the incident energy is, hence, deposited in the lower-density region, and the number of the particles which contribute to soft x-ray emission decreases. We can estimate the density scale-length L for an assumed density profile. For an exponential profile of $n_e = n_c \exp(-x/L)$, where n_e and n_c are the electron density and the critical density, respectively, and x is the coordinate along the plasma density gradient, the absorption fraction f_A for the inverse bremsstrahlung is given by[26]

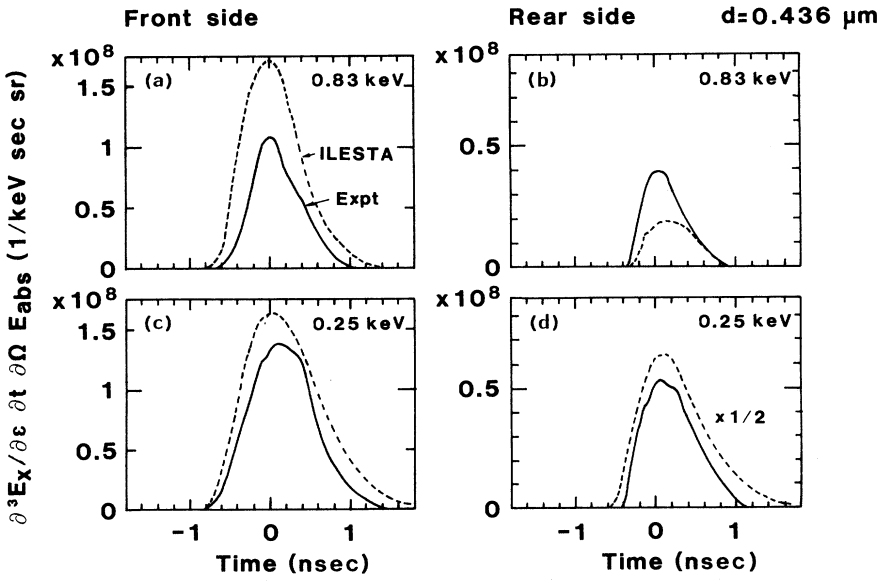

FIG. 12. Temporal variations of the emission at the front side (a) and (c) and th rear side (b) and (d). For comparison, the simulated emission intensity of 0.25 keV at the rear side is multiplied by $\frac{1}{2}$.

$$f_A = 1 - \exp(-a_0 \cos^2\theta) , \quad (2)$$

where θ is the incidence angle and a_0 is the absorption coefficient for normal incidence:

$$a_0 = 8\nu_{EI}^* L/3c . \quad (3)$$

Here ν_{EI}^* is the electron-ion collision frequency evaluated at the critical density and c is the velocity of light. As seen from the thin solid curves in Fig. 3, the estimated absorption fits to data points for the value of $a_0 = 5$. Using an electron temperature of 2 keV and an ion charge Z of 60, which are the typical values taken from the ILESTA simulation, we estimated ν_{EI}^* and obtained a scale length of $L \sim 6$ μm. Such a scale length has already been noted by many authors.[1,4]

The dominant region for x-ray emission does not directly correlate with the energy-deposition region. In fact, the measured x-ray-conversion rate was independent of the incidence angle up to 50°, although the plasma density at the turning point of laser light is proportional to $\cos^2\theta$ for the assumed plasma profile.

B. Radiation heat transport in a gold-foil target

X-ray emissions at the front and rear sides of the gold foil are related closely with radiation heat conduction. The absorbed laser energy is transported predominantly by x-ray radiation producing an ablation region between the critical density region and the ablative front where the temperature sharply decreases. As time proceeds, the heat front propagates to the rear side and the depth of the cold region at the rear side becomes thin enough to transmit the radiation toward the target rear side, where it emerges.

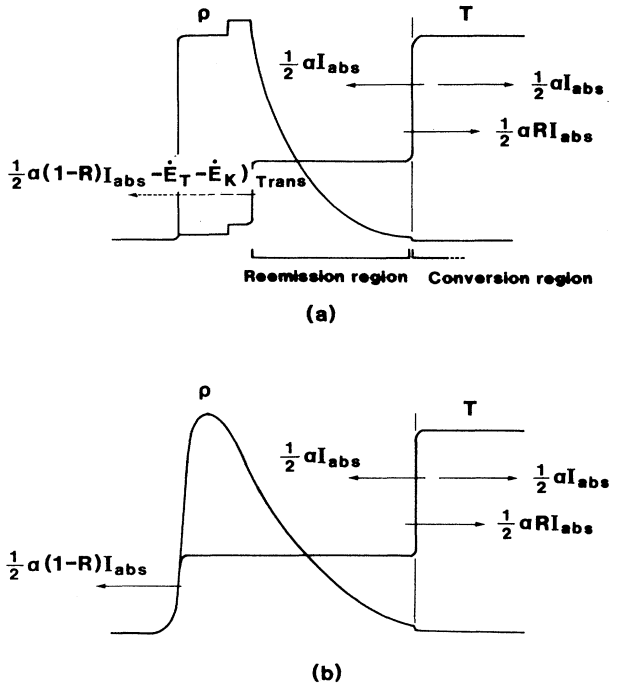

FIG. 13. Temperature (T) and density (ρ) profiles of the laser-heated gold foil are shown schematically. These are profiles (a) before and (b) after the occurrence of foil burnthrough driven by the radiation heat wave.

We can interpret the above situation by adopting the models developed by Pakula and Sigel[10] and Sigel *et al.*[27] First, we assume two separate regions as shown in Fig. 13. The total flux I_x^F radiated toward the front side (the side of laser incidence) is given by

$$I_x^F = \tfrac{1}{2}\alpha(1+R)I_{abs} , \quad (4)$$

where α is the x-ray conversion rate, R is the reflectivity (the fractional radiant energy reemitted from the ablation region), and I_{abs} is the absorbed laser flux. The remaining energy flux is equal to the sum of the time derivatives of the thermal energy $\dot{E}_T$, the kinetic energy of the ablation region $\dot{E}_k$, and the radiative losses toward the rear side I_x^R:

$$\dot{E}_T + \dot{E}_k + I_x^R = \tfrac{1}{2}\alpha(1-R)I_{abs} . \quad (5)$$

Thus the net flux I_{HW} driving the ablation is given by

$$I_{HW} = \dot{E}_T + \dot{E}_k = \tfrac{1}{2}\alpha(1-R)I_{abs} - I_x^R . \quad (6)$$

During the early stages, the target rear side is cold and optically thick enough to absorb the radiation totally (i.e., $I_x^R = 0$) and the heat wave propagates toward the rear side. When the burn through of the radiation heat wave occurs, the radiative loss at the rear side increases markedly, the net heat flux I_{HW} decreases due to radiative cooling, and R asymptotically approaches 0.5 as much as the reemission region is optically thick. If the reemission region becomes optically thin, this region does not reemit the radiation any more. Then R approaches 0.

Let us estimate the conversion rate α and the reemission coefficient R for the measurements described above in order to calculate the time dependence of the x-ray emission at the front and rear sides of the target. We consider the case of the large-spot experiment. Figure 14(a) shows x-ray-emission intensities as determined from the brightness temperatures, which give the same intensity values for both the experimental result and corresponding Planckian distribution in the common spectral region of 10–100 Å. If $\dot{E}_T$ and $\dot{E}_k$ are negligibly small (i.e., steady state), the relations of Eqs. (4) and (5) become

$$\tfrac{1}{2}\alpha(1+R) = I_x^F/I_{abs} , \quad (7)$$

$$\tfrac{1}{2}\alpha(1-R) = I_x^R/I_{abs} , \quad (8)$$

This simplification is valid after the burn through occurs. It is shown below that the source radiation intensity ($=\alpha I_{abs}/2$) becomes equal to the radiation loss toward both the front and rear sides, and consequently that the net heat flux I_{HW} approaches zero. Using the temporal peak values, we obtain $\alpha = 0.73$, $R = 0.46$, and the source radiation flux of $I_x^S = \tfrac{1}{2}\alpha I_{abs} = 1.1 \times 10^{14}$ W/cm^2 at the intensity maximum.

In order to calculate the x-ray-emission intensity, the ablation velocity and the temperature of the ablative region must be obtained. The self-similar solutions under the boundary condition of constant source flux predicts the mass ablation rate for gold to be[10]

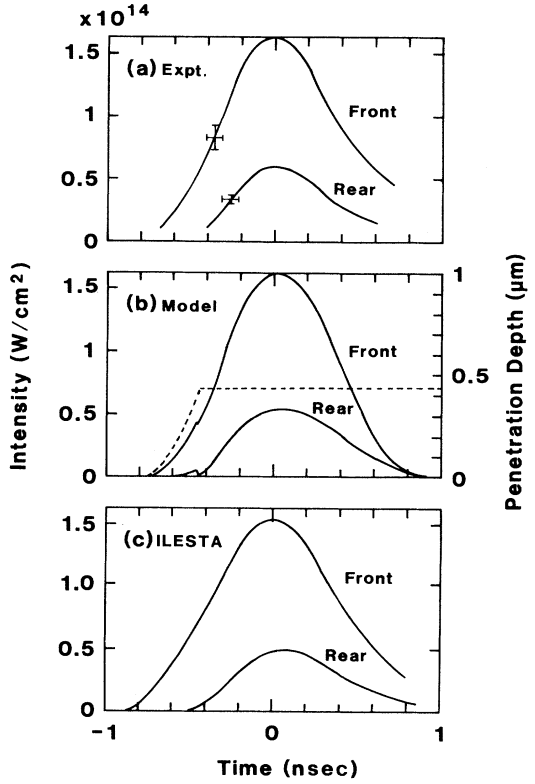

FIG. 14. Time history of x-ray emission at the front and rear sides of the thin gold foil of 0.436-μm thickness. (a) Experiment, (b) numerical calculation based on the self-similar solutions, and (c) ILESTA simulation. The calculated penetration depth of the ablation region formed by the radiation heat wave is represented by a dashed line.

$$\dot{m}=4.7\times10^{6}\hat{I}_{\rm HW}^{7/13}\hat{t}^{-3/13}\ ({\rm g/cm^2\,s})\ , \tag{9}$$

where $\hat{I}_{\rm HW}$ is the net heat flux in units of 10^{14} W/cm^2, and $\hat{t}$ is the time in units of 10^{-9} s. The temperature of the ablation region is derived from the energy deposited in this region ($E_{\rm tot}$) and the total ablated mass during source flux injection.

Finally, we need a quasi-steady-state approximation for the ablation-depth calculation because Eq. (9) is available for a steady-state case. Therefore, we define the effective injection time $\tau(t)$ until the instant when the deposited energy at the constant range of $I_{\rm HW}(t)$ becomes equal to the total energy in the ablation region,

$$E_{\rm tot}(t)=\int_0^t I_{\rm HW}(t')dt'=\tau(t)I_{\rm HW}(t)\ . \tag{10}$$

The radiation flux from the reemission region is calculated on the assumption of black-body emission; i.e., σT^4, where σ is the Stefan-Boltzmann constant. Hence, the emission intensity at the target front side is given by $I_x^S+\sigma T^4$. The emission at the target rear side is the transmitted component $I_x^R=\int\eta(\varepsilon)\Phi_T(\varepsilon)d\varepsilon$, where $\eta(\varepsilon)$ is the transmission of x rays at the photon energy of ε (keV) and $\Phi_T(\varepsilon)$ is the Planckian for the temperature of T. $\eta(\varepsilon)$ is also calculated by using the approximated formula of the absorption cross section for the bound-free transitions,[28]

$$\sigma_{\rm BF}=4.87\times10^{-15}\varepsilon^{1.05}\exp[-0.168(\ln\varepsilon+6.91)^2]\ ({\rm cm^2})\ . \tag{11}$$

The temporal shape of the source flux was chosen to be the experimental average.

The calculated result of Fig. 14(b) shows the x-ray emission from each side (solid lines) and the penetration depth of the radiation heat wave (dashed line). The model replicates the experiment well except for the falling part of the front-side emission. The radiation heat wave arrives to the rear side 450 ps prior to the time of signal peak at the front side. The x-ray intensity then decreases slightly due to an increase in radiation cooling at the rear side. The ratio of the front-side to rear-side emission intensities is about 3. Consequently the net heat flux and the emission flux balance after the burnthrough of the radiation heat wave.

For the optically thick, isothermal reemission region, R becomes 0.5 and we obtain $I_x^F/I_x^R=(1+R)/(1-R)=3$ from the relation of Eqs. (7) and (8). By contrast, this ratio becomes unity for the optically thin case for which $R=0$.

High x-ray-emission intensity from the rear side of a foil might be useful as an x-ray source. Computational studies made with the ILESTA code used in this study can suggest an optimum foil thickness thick enough to stop the burnthrough by the laser beam, while thin enough to obtain the highest x-ray conversion at the rear side. With this value, nearly 30% of the incident laser energy is converted to the x-ray emitted at the rear side.

C. Miscellanies

Comparing experimental results of the O-band emission at the front side of the thin gold foil with the simulation we note better agreement for the large-laser-spot case than that for the small-spot case. This can be understood if the O-band and N-band emissions are produced in different regions at the target. For a planar geometry, the hot region at the laser spot is surrounded by a relatively cold region extending laterally away from the beam focus, and axially into the dense region behind the ablation front. The O-band emission, produced primarily in the hot region, may then be affected by the size of the laser spot and the duration of the laser pulse, due to the lateral transport effect. This explanation is supported by experimental evidence that the emission source size of the O-band emission is found to be much larger than that of the N-band emission[29] which corresponds to the laser spot size, and that the instantaneous x-ray-conversion rate of the O-band emission component grows faster than that of the N-band emission[3] for long-pulse laser irradiation.

As discussed in the previous sections, the non-LTE code ILESTA-1D can predict well the laser intensity dependence of x-ray-conversion rate and radiation transport

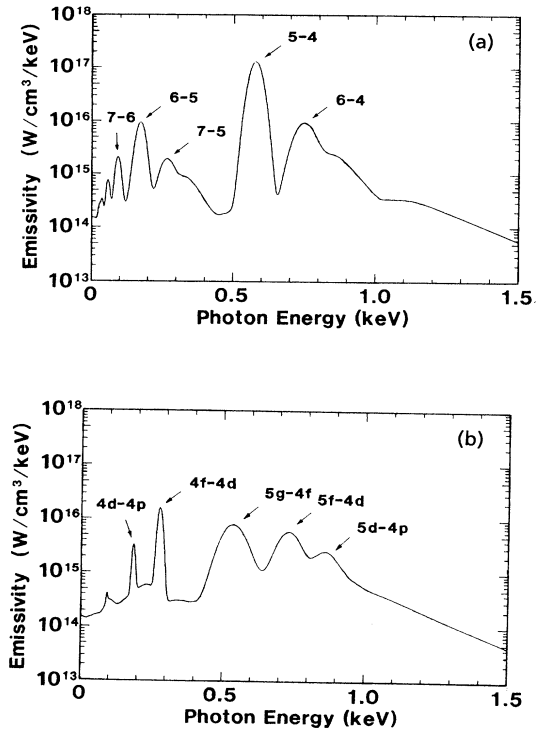

FIG. 15. An example of gold emissivities calculated for a density of 0.1 g/cm^3 and an electron temperature of 200 eV. (a) Bound-bound transitions between the levels determined by only the principal quantum number are considered in the average ion model adopted in the ILESTA code, and (b) sublevels arising from the l splitting are taken into account.

phenomena. However, even in the case of the large-spot-size experiment, where the dynamics is expected to be sufficiently one dimensional, the x-ray spectra is not well reproduced with the present code [see Fig. 11(a)]. A typical feature seen in the experimental spectra is (1) a strong peak around 220 eV and (2) an almost flat shelf from 400 to 800 eV. However, the ILESTA provides two peaks around 250 and 700 eV, stemming from the O-band and N-band emission, respectively. Such a feature of numerical spectra strongly depends upon the atomic model. In the present model, only the line radiations due to transitions with differences in the principal quantum number are included, and no inner-shell transitions as well as no angular-momentum dependence are modeled. The x-ray spectra obtained in a simulation are very sensitive to the atomic model with which the emissivity and opacity of radiation transport are evaluated.

Photon-energy dependence of the emissivity used in the present simulation code is shown in Fig. 15(a) for the case of temperature 200 eV and density 0.1 g/cm^3. The N-band emission stems from the transition of $n=5$ to $n=4$, while the O-band stems from that of $n=6$ to $n=5$. It is noted that the line shape has been modified with the effective width described in Sec. II. On the other hand, the inclusion of the l-splitting effect alters the spectra drastically. The N-band due to the 5-4 transition is separated into three lines $5g$-$4f$, $5f$-$4d$, and $5d$-$4p$. These lines are found to make a broad shelf with the width of about 400 eV. This is seen in Fig. 15(b). It is obvious that for high-Z, partially ionized atoms, the atomic model without the l-splitting effect is a very rough model to predict the x-ray spectra. In addition, new lines which are not principally included in the model without l splitting appear to be important. They are line radiations stemming from $4f$-$4d$ and $4d$-$4p$ transitions. The $4f$-$4d$ line especially has a strong peak near 250 eV, and can be considered to be a remarkable candidate in explaining the strong peak in the experimental spectra. More details, including simulation results with such a new model, will be published elsewhere.[30]

V. CONCLUSIONS

X-ray emission and transport in the case of gold plasmas generated by intense laser light have been investigated. Absolute x-ray-emission spectra with high spectral resolution were accurately measured. Plasmas of spherical geometry or large lateral extent were produced to minimize effects arising from plasma boundaries which make difficult the comparison between experiment and model calculation. The calculated x-ray intensities in the sub-keV region have been found to be in good agreement with the experimental results, while the spectral shape did not agree sufficiently with the measurement, and in particular, with the experimentally observed N-band emission.

We have measured the laser-light absorption and the x-ray-conversion rates as a function of the laser incidence angle. The absorption and the conversion rates have shown very weak dependence on the angle up to 50°, but both values rapidly decrease as the incidence angle increases. The estimated plasma density and the scale length cannot completely explain the angular dependence of the x-ray conversion, which suggests existence of another x-ray-emission region separate from the laser turning region.

The intensity dependence of x-ray conversion of a spherical target heated uniformly by multiple laser beams quantitatively shows good agreement with the simulation results as well as with the results of similar experiments. It has been shown that the observed spectra mainly consists of O lines and N lines of gold, which are identified by comparison with the simulated spectrum. The intensity of the O-band emission markedly decreases with an increase in the laser intensity, while the intensity of the N-band emission shows somewhat weak dependences. These features are not completely tracked by ILESTA simulations.

The absolute x-ray-emission spectra from the laser-irradiated thin gold-foil targets have been studied. From temporal and spectral behavior of the rear-side emission, we may infer the radiation hydrodynamics of a gold foil. Emission intensities at the front side of the target are well reproduced by the simulation, but the intensities at the rear side are not. This discrepancy is likely due to the treatment of radiative transition lines adopted in the ILESTA code. A preliminary study on the l-splitting effect on the absorption and emission of radiation suggests qualitatively an explanation for the discrepancy.

X-ray emission at the front and rear sides of the target was analyzed by the self-similar solutions presented by Pakula and Sigel. Numerically obtained x-ray emission at the front and rear sides, by using the approximated gold opacity under LTE conditions and the quasistationary approximation offered in this work, show good agreement with the observation.

ACKNOWLEDGMENTS

The authors would like to thank T. Yabe for his suggestion and simulation study on radiation transport in a gold foil. We acknowledge the help and support of many people who contributed in various ways to this work. We especially appreciate support from T. Yamanaka, M. Nakatsuka, T. Jitsuno, K. Yoshida, T. Norimatsu, M. Takagi, and C. Yamanaka. We have benefited from the spectrometer calibration performed through collaborative work with K. Taniguchi and K. Toyoda. Finally, this work could not have been completed without technical assistance of the GOD, OT, M, and T groups of Institute of Laser Engineering, Osaka University. All of their contributions are gratefully acknowledged.

[1]W. C. Mead, E. K. Stoner, R. L. Kauffman, H. N. Kornblum, and B. F. Lasinski, Phys. Rev. A **38**, 5275 (1988).

[2]R. Kodama, K. Okada, N. Ikeda, M. Mineo, K. A. Tanaka, T. Mochizuki, and C. Yamanaka, J. Appl. Phys. **59**, 305 (1986).

[3]F. Ze, D. R. Kania, S. H. Langer, H. Kornblum, R. Kauffman, J. Kilkenny, E. M. Campbell, and G. Tietbohl, J. Appl. Phys. **66**, 1935 (1989).

[4]P. D. Goldstone, S. R. Goldman, W. C. Mead, J. A. Cobble, G. Stradling, R. H. Day, A. Haner, M. C. Richardson, R. S. Marjoribanks, P. A. Jaanimagi, R. L. Keck, F. J. Marshall, W. Seka, O. Barnouin, B. Yaakobi, and S. A. Letzring, Phys. Rev. Lett. **59**, 56 (1987).

[5]T. Mochizuki, T. Yabe, K. Okada, M. Hamada, N. Ikeda, S. Kiyokawa, and C. Yamanaka, Phys. Rev. A **33**, 525 (1986).

[6]K. Eidmann, T. Kishimoto, P. Hermann, J. Mizui, R. Pakula, R. Sigel, and S. Witkowski, Lasers Part. Beams **4**, 521 (1986).

[7]H. Nishimura, F. Matsuoka, M. Yagi, K. Yamada, S. Nakai, G. H. McCall, and C. Yamanaka, Phys. Fluids **26**, 1688 (1983).

[8]P. Celliers and K. Eidmann, Phys. Rev. A **41**, 3270 (1990).

[9]T. Mochizuki, K. Mima, N. Ikeda, R. Kodama H. Shiraga, K. A. Tanaka, and C. Yamanaka, Phys. Rev. A **36**, 3279 (1987).

[10]R. Pakula and R. Sigel, Phys. Fluids **28**, 232 (1985); **29**, 1340 (E) (1986).

[11]G. D. Tsakiris and K. Eidmann, J. Quant. Spectrosc. Radiat. Transfer **38**, 353 (1987).

[12]For example, see D. Mihalas and B. W. Mihalas, *Foundations of Radiation Hydrodynamics* (Oxford University, New York, 1984); Ya. B. Zel'dovich and Yu. P. Raizer, *Physics of Shock Waves and High Temperature Hydrodynamics Phenomena* (Academic, New York, 1966); G. C. Pomraning, *The Equation of Radiation Hydrodynamics* (Pergamon, Oxford, 1973).

[13]H. Takabe, M. Yamanaka, K. Mima, C. Yamanaka, H. Azechi, N. Miyanaga, M. Nakatsuka, T. Jitsuno, T. Norimatsu, M. Takagi, H. Nishimura, M. Nakai, T. Yabe, T. Sasaki, K. Yoshida, K. Nishihara, Y. Kato, Y. Izawa, T. Yamanaka, and S. Nakai, Phys. Fluids **31**, 2884 (1988).

[14]S. Skupsky, Phys. Rev. A **36**, 5701 (1987).

[15]L. Spitzer and R. Härm, Phys. Rev. **89**, 977 (1953).

[16]For example, see H. L. Wilson, *Progress in High Temperature Physics and Chemistry* (Pergamon, Oxford, 1972), Vol. 5, p. 125.

[17]H. Mayer, "Method of opacity calculations," Los Alamos Scientific Laboratory Report No, LA-647, Los Alamos, NM, 1947 (unpublished).

[18]R. M. More and J. Quant. Spectrosc. Radiat. Transfer **27**, 345 (1982).

[19]M. Itho, T. Yabe, and S. Kiyokawa, Phys. Rev. A **35**, 233 (1987).

[20]C. Yamanaka, Nucl. Fusion **25**, 1343 (1985).

[21]W. Schwanda and K. Eidmann, Appl. Opt. (to be published).

[22]B. L. Henke, S. L. Kwok, J. Y. Uejio, H. T. Yamada, and G. C. Young, J. Opt. Soc. Am. B **1**, 818 (1984).

[23]B. L. Henke, F. G. Fujiwara, M. A. Tester, C. H. Dittmore, and M. A. Palmer, J. Opt. Soc. Am. B **1**, 828 (1984).

[24]S. Uchida, M. Tanaka, Y. Sakawa, H. Nishimura, T. Yamanaka and C. Yamanaka, Rev. Sci. Instrum. **56**, 1867 (1986).

[25]K. Estabrook and W. L. Kruer, Phys. Rev. Lett. **40**, 42 (1978).

[26]W. L. Kruer, *The Physics of Laser Plasma Interactions,* from the series *Frontiers in Physics,* edited by D. Pines (Addison-Wesley, Reading, MA, 1987), p. 51.

[27]R. Sigel, K. Eidmann, F. Lavarenne, and R. F. Schmalz, Phys. Fluids B **2**, 199 (1990); K. Eidmann, R. F. Schmalz, and R. Sigel, *ibid.* **2**, 208 (1990).

[28]T. Yabe, S. Kiyokawa, and H. Nishimura, Jpn. J. Appl. Phys. **24**, L439 (1985).

[29]M. Chaker, V. Bareau, J. C. Kieffer, H. Pépin, and T. W. Johnston, Rev. Sci. Instrum. **60**, 3386 (1989).

[30]T. Nishikawa and H. Takabe (unpublished).

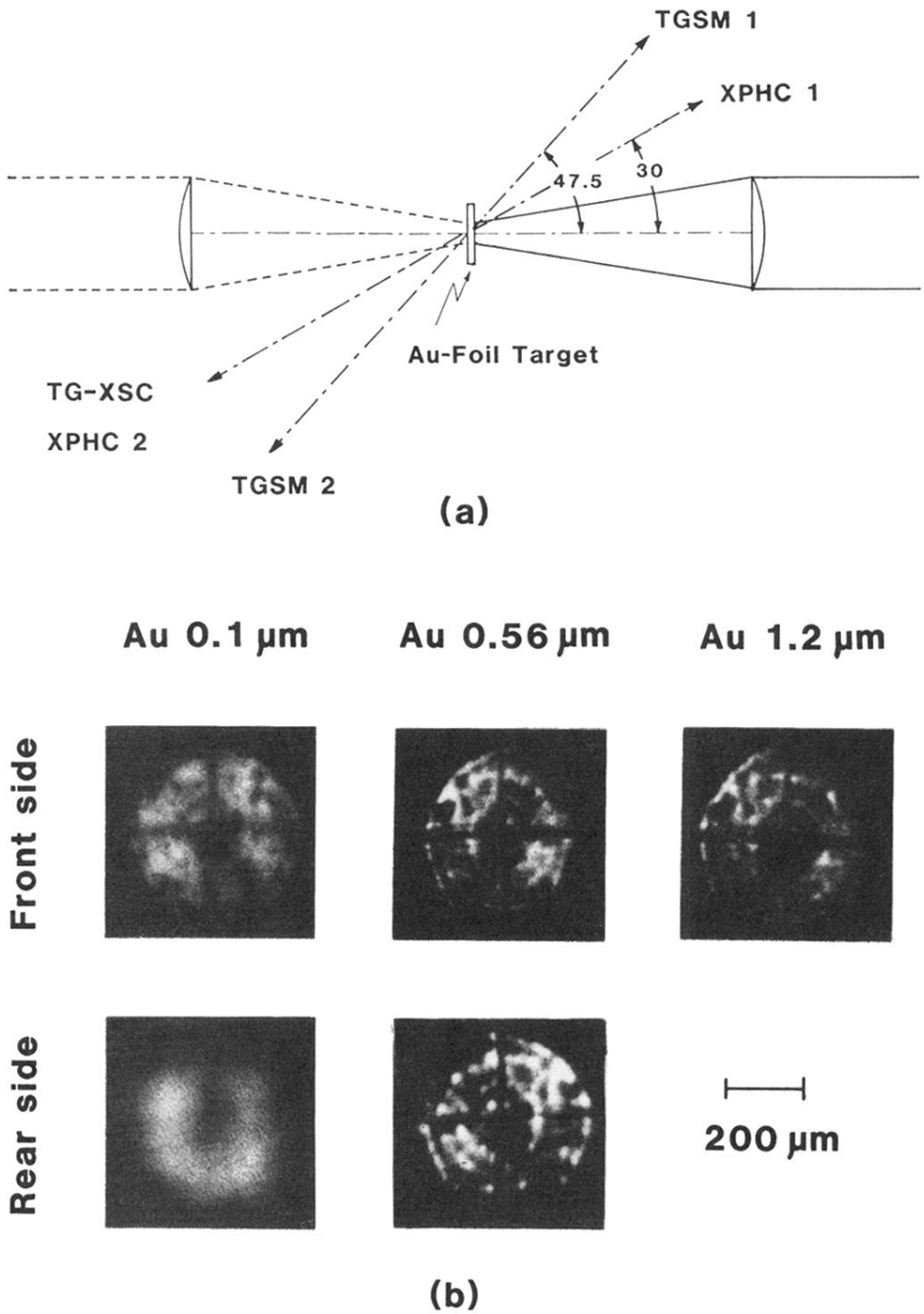

FIG. 6. (a) Experimental setup for thin gold-foil irradiation with a relatively small size of laser spot (430-μm diam). Laser intensity was 1.5×10^{14} W/cm^2. Diagnostic instruments were transmission grating spectrometers with film (TGSM's), a transmission grating with an x-ray streak camera (TG-XSC), and the x-ray pinhole camera (XPHC). The two laser beams were used alternatively throughout the shot sequence. (b) X-ray pinhole pictures at the same irradiation for three different foil thicknesses. X-ray spectral range was 2–4 keV.